Electronic Supplementary Material (ESI) for Energy & Environmental Science.

Supporting Information

$Li_{0.6}[Li_{0.2}Sn_{0.8}S_2]$ – A layered lithium superionic conductor

T. Holzmann[†‡§], L. M. Schoop[†], M. N. Ali[*], I. Moudrakovski[†], G. Gregori[†], J. Maier[†], R. J. Cava[*], B. V. Lotsch[†‡§]*

[†]Max-Planck-Institute for Solid State Research, Heisenbergstr. 1, 70569 Stuttgart, Germany

[‡]Department of Chemistry, Ludwig-Maximilians-Universität München, Butenandtstr. 5-13, 81377 München, Germany

[§]Nanosystems Initiative Munich (NIM) & Center for Nanoscience, Schellingstr. 4, 80799 München, Germany

[*]Department of Chemistry, Princeton University, Princeton, NJ 08544, USA.

Synthesis: Polycrystalline $Li_{0.6}[Li_{0.2}Sn_{0.8}S_2]$ was synthesized using three different routes. Synthesis 1 was already reported by *Kuhn* et *al.* and is described in ref. 1. For synthesis 2, Li_2CO_3 (Alfa Aesar, 99.0 % min), SnS_2 (Johnson Matthey Electronics brand, 99.5 % metals basis) and S (Alfa Aesar, 99.5 %) were mixed in a stoichiometric ratio with a slight excess of sulfur (2 wt% with regard to the product). Synthesis 3 uses a stoichiometric amount of Li_2S (Alfa Aesar, 99.9 %), SnS_2 (Johnson Matthey Electronics brand, 99.5 % metals basis) and S (Alfa Aesar, 99.5%). For $Li[Li_{0.33}Sn_{0.67}S_2]$, all synthesis procedures gave the same material according to NMR and PXRD. In the case of $Li_{0.6}[Li_{0.2}Sn_{0.8}S_2]$, synthesis 1 resulted in an amorphous side phase detected by NMR, which could be avoided by using syntheses 2 or 3. The starting materials were thoroughly ground and vacuum-sealed in silica tubes within a carbon crucible – this carbon crucible prevents the reaction of lithium with the silica tube and in the case of synthesis 2 it further reduces the Li_2CO_3 and therefore prevents formation of the oxide compound. For reaction 2 and 3 a furnace was heated to 700 °C (120 °C h^{-1}), held at that temperature for 3 days and then cooled down to room temperature (180 °C h^{-1}). All preparation steps were carried out under inert atmosphere or vacuum.

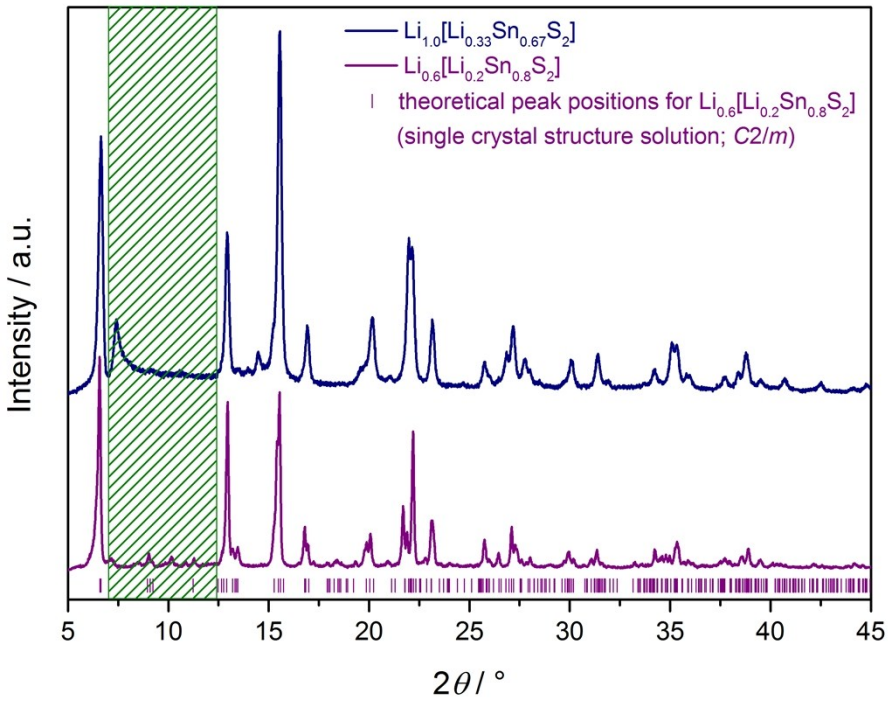

Figure S1. Mo-K_α PXRD pattern of $Li_{0.6}[Li_{0.2}Sn_{0.8}S_2]$ (bottom, purple) in comparison with $Li[Li_{0.33}Sn_{0.67}S_2]$ (top, blue). The purple scatter mark the theoretical peak positions of $Li_{0.6}[Li_{0.2}Sn_{0.8}S_2]$, according to the single crystal structure solution. The reflections in the highlighted region of 7-12 °2θ belong to the monoclinic superstructure cell. Differences between single crystal structure solution and powder X-ray data arise from varying concentrations of stacking faults in the powder.

Table S1. Atomic coordinates of the single crystal structure solution of $Li_{0.6}[Li_{0.2}Sn_{0.8}S_2]$.

Site	Wyck.	*x*	*y*	*z*	*occ.*
Sn1	2b	0	1/2	0	0.625
Li1A	2b	0	1/2	0	0.375
Sn2	4i	0.16471(2)	0	0.99600(7)	0.872
Li2A	4i	0.16471(2)	0	0.99600(7)	0.128
S3	4i	0.91344(7)	1/2	0.2420(2)	1
S4	4i	0.08395(8)	0	0.2351(2)	1
S5	4i	0.25193(8)	0	0.7669(2)	1
Li3	4i	0.8360(9)	1/2	0.502(3)	0.58
Li4	2c	0	0	1/2	0.3
Li5	4i	0.0391(18)	1/2	0.340(6)	0.216

Table S2. Anisotropic displacement parameters of the single crystal structure solution of $Li_{0.6}[Li_{0.2}Sn_{0.8}S_2]$.

Anisotropic displacement parameters, in Å^2				
Atom	U_{11}	U_{22}	U_{33}	U_{13}
Sn1	0.0033(4)	0.0050(4)	0.0095(5)	0.0022(3)
Li1A	0.0033(4)	0.0050(4)	0.0095(5)	0.0022(3)
Sn2	0.0061(2)	0.0053(2)	0.0126(3)	0.00492(16)
Li2A	0.0061(2)	0.0053(2)	0.0126(3)	0.00492(16)
S3	0.0128(8)	0.0106(7)	0.0147(8)	0.0034(6)
S4	0.0142(8)	0.0174(7)	0.0131(8)	0.0075(6)
S5	0.0102(7)	0.0093(7)	0.0117(8)	0.0067(5)
Li3	0.028(10)	0.010(9)	0.014(11)	0.003(7)
Li4	0.01100	0.00700	0.02100	0.00600
Li5	0.01500	0.00800	0.01300	0.00100

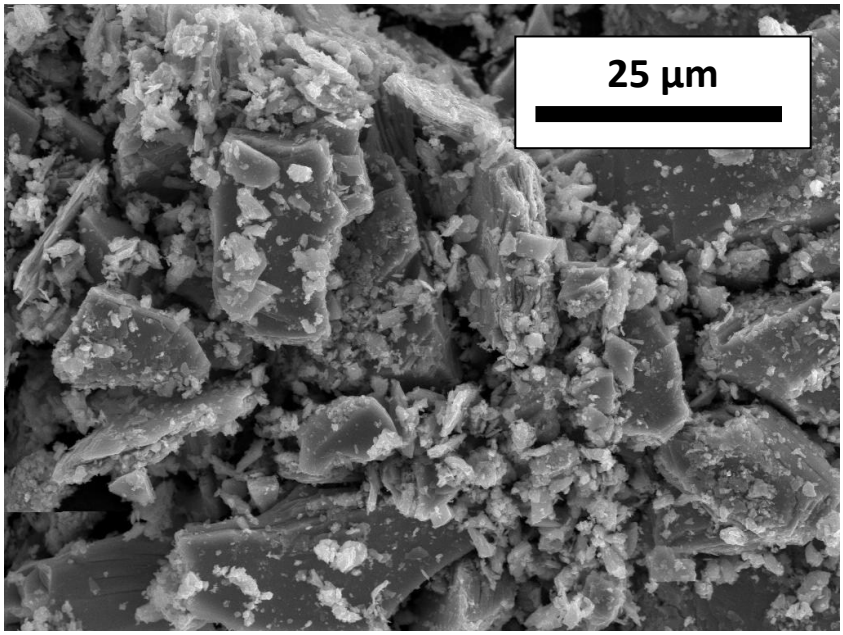

Figure S2. SE-SEM image (20 kV) of a typical $Li_{0.6}[Li_{0.2}Sn_{0.8}S_2]$ powder with a grain size in the range of <1µm – 100 µm.

Table S3. EDX data of $Li_{0.6}[Li_{0.2}Sn_{0.8}S_2]$ crystals.

Spectrum	**S**	**Sn**
Expected	71.43	28.57
Spectrum 1	70.60	29.40
Spectrum 2	70.59	29.41
Spectrum 3	70.14	29.86
Spectrum 4	70.55	29.45
Spectrum 5	70.69	29.31
Mean	70.51	29.49

Table S4. ICP-AES data of $Li_{0.6}[Li_{0.2}Sn_{0.8}S_2]$ in atomic- and weight-%. Two measurements of each sample were performed.

$Li_{0.6}[Li_{0.2}Sn_{0.8}S_2]$	**Li**	**Sn**
wt%	2.83 2.80	50.42 50.79
at%	1.0 1.0	1.04 1.08
Expected (at%)	1.0	1.0

Solid-state NMR spectroscopy

Experimental Details: ^{6}Li and ^{119}Sn SS NMR spectra were obtained on a Bruker Avance III 400 MHz instrument (B_0 = 9.4 T) at Larmor frequencies of 400 MHz, 58.88 MHz and 149.12 MHz, respectively. All measurements were performed with a Bruker 4 mm triple-channel Magic Angle Spinning (MAS) probe in ZrO_2-spinners at spinning speeds between 5 kHz and 14 kHz. In most cases the spectra were collected using a simple Bloch decay ($\pi/2$-pulse-acquire-delay) with $\pi/2$-pulses for ^{6}Li and ^{119}Sn set to 5.8 μs (B_1 = 43.1 kHz) and 4 μs (B_1 = 62.5 kHz), respectively. ^{119}Sn spectra are externally referenced to neat tetramethyltin ($Sn(CH_3)_4$, δ_{iso} = 0.0 ppm) with solid SnO_2 used as a secondary chemical shift standard (δ_{iso}-603.0 ppm relative to $Sn(CH_3)_4$).[2] ^{6}Li spectra are referenced to a 9.7 M aqueous solution of LiCl (δ_{iso} = 0.0 ppm).[2] ^{6}Li spectra employed delays between 30 and 500 s, and ^{119}Sn experiments used delays between 200 and 400 s. In every case the relaxation delays were set to provide for quantitative spectra, which was validated by the estimates of the relaxation times performed for every specific situation. The temperature of the samples in the MAS experiments was controlled using a Bruker BVT3000 temperature controller and was calibrated using the ^{207}Pb signal in $Pb(NO_3)_2$.[3] Analytical simulations and integration of experimental spectra were carried out with the DMFit and Bruker TopSpin 3.2 Lineshape Analysis Tool simulation packages.[4,5]

^{119}Sn NMR:

^{119}Sn NMR measurements were performed on $Li[Li_{0.33}Sn_{0.67}S_2]$, $Li_{0.6}[Li_{0.2}Sn_{0.8}S_2]$ as well as on SnS_2 for comparison. As expected due to the high crystallinity and the well-defined tin environment, SnS_2 gave a single signal at -764.7 ppm (Figure S3).

^{119}Sn NMR of $Li[Li_{0.33}Sn_{0.67}S_2]$ displays one signal at -765.9 ppm, which is slightly shifted compared to SnS_2, indicating less shielding at the tin atoms in $Li[Li_{0.33}Sn_{0.67}S_2]$ (Figure S5). As both crystallographic tin positions in $Li[Li_{0.33}Sn_{0.67}S_2]$ have the same chemical environment, the single signal is in good agreement with our expectations.

$Li_{0.6}[Li_{0.2}Sn_{0.8}S_2]$ shows three ^{119}Sn NMR peaks at -747.6 ppm, -750.1 ppm and -754.6 ppm with an integral ratio of around 39 : 21 : 40. According to the literature[6,7] this chemical shifts proves that only Sn(+IV) atoms are present, which are presumably all octahedrally coordinated by sulfur. Sn(+II) would show signals with a much smaller chemical shift. According to the crystal structure solution there are two crystallographically different Sn atoms. 26 % of all Sn atoms are located on the position Sn1 whereas 74% are located on Sn2. As the first coordination sphere is octahedrally coordinated sulfur for both tin positions, a clear assignment of the peaks cannot be made. Nevertheless, with respect to the integral ratios it seems likely that the two peaks at -747.6 ppm and -754.6 ppm belong to Sn2 with an integral sum of 79 % and the third peak at -750.1 ppm belongs to Sn1 with an integral of 21 %. As we expect a ratio of 26 : 74 for Sn1 : Sn2 this is in quite good agreement. This assumption is further confirmed by low temperature measurements, as the two Sn2 peaks are shifted to higher negative ppm values and the Sn1 peaks remains at -750.1 ppm. As we have lithium motion in the sample and the crystal structure solution gives us mixed occupancies we assume that the splitting into two peaks for the Sn2 position arises from small differences in local chemical environments, e.g. differences in the second coordination sphere (one, two or more Li atoms, see Figure S7) or slightly distorted sulfur octahedra. A similar situation was previously observed in powdered SnS_2 where several signals in the range of -755 ppm to -780 ppm appeared, mainly due to different stacking periodicities and distortions.[6]

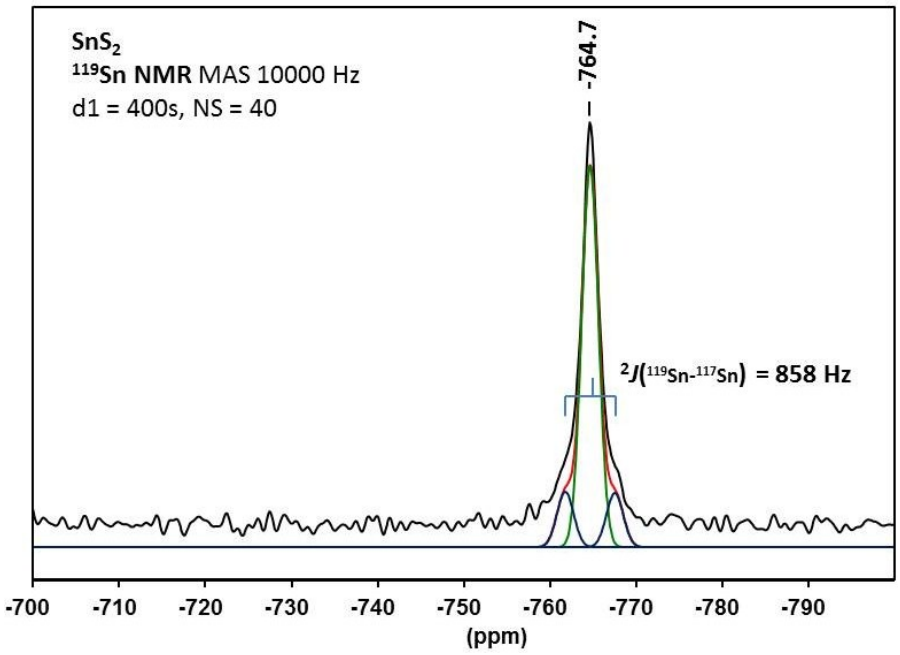

Figure S3. ^{119}Sn NMR spectrum of SnS_2 flakes ground with glass powder. The black line corresponds to the measured spectrum, the red line corresponds to the overall fit out of the single curves (in blue and green). The shoulders belong to a ^{119}Sn-^{117}Sn scalar coupling.

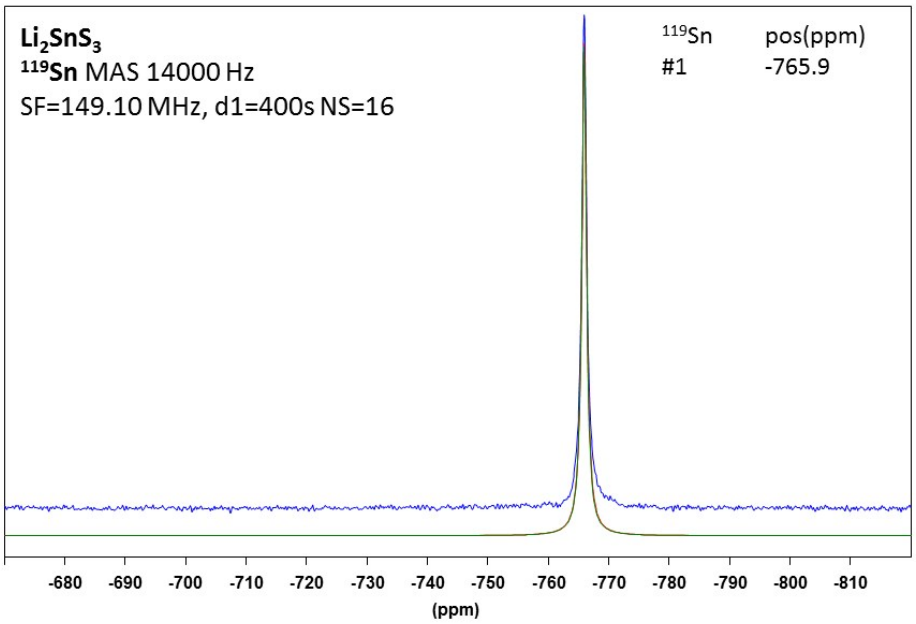

Figure S4. ^{119}Sn NMR spectrum of $Li[Li_{0.33}Sn_{0.67}S_2]$. In blue: measured spectrum, in green: single fit and in red: overall fit.

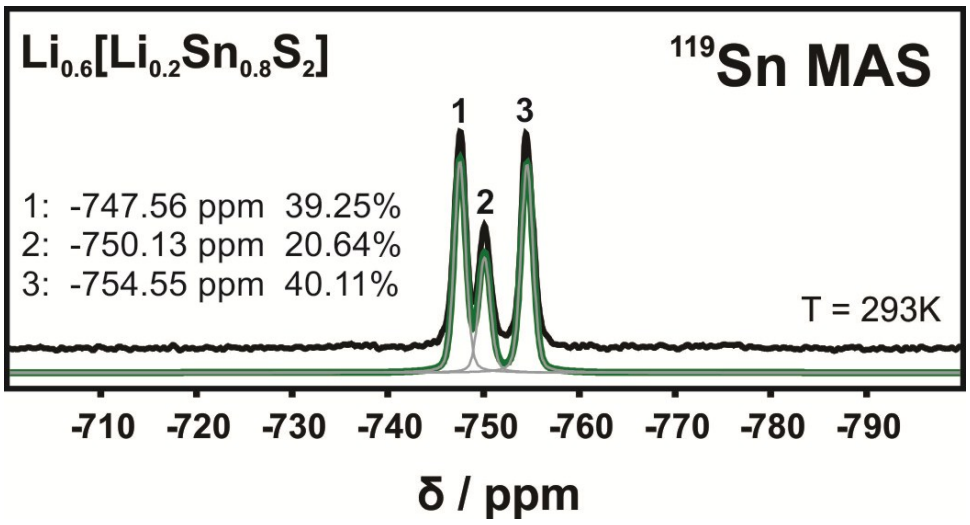

Figure S5. ^{119}Sn NMR spectrum of $Li_{0.6}[Li_{0.2}Sn_{0.8}S_2]$. In black: measured spectrum, in green: overall fit, in grey: single fits.

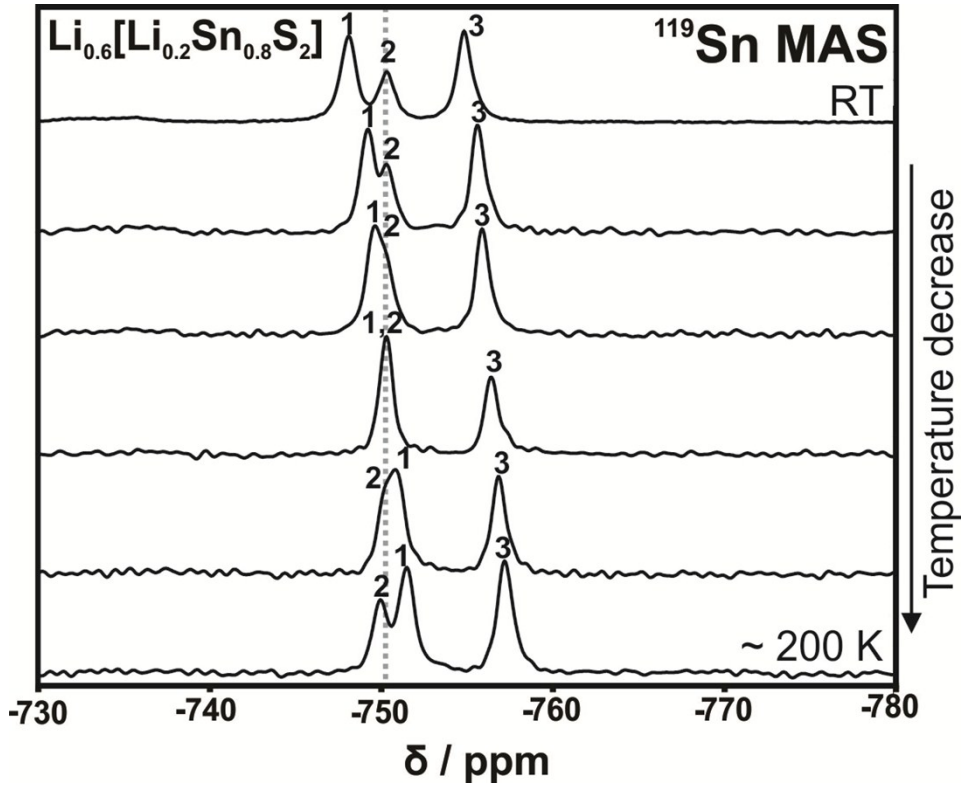

Figure S6. ^{119}Sn NMR spectrum of $Li_{0.6}[Li_{0.2}Sn_{0.8}S_2]$ at varying temperatures. Temperature is decreased downwards. Note that only peak 1 and peak 3 are highfield shifted with a decreased temperature, indicating that both peaks belong to the same tin position.

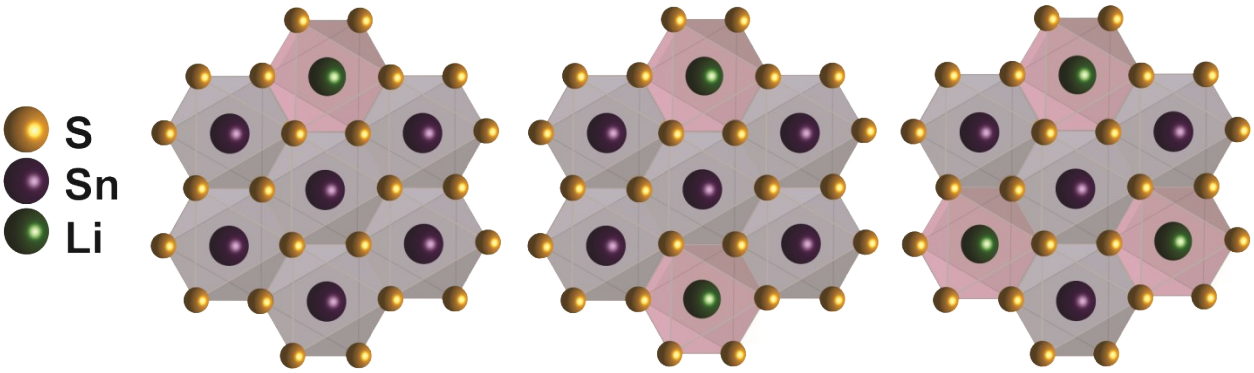

Figure S7. Schematic representation of three possible chemical environments of the tin atoms in the covalent layers of $Li_{0.6}[Li_{0.2}Sn_{0.8}S_2]$ surrounded by one (left), two (middle) or three (right) lithium atoms. Not that these are just examples which do not necessarily occur in the material with the same abundance.

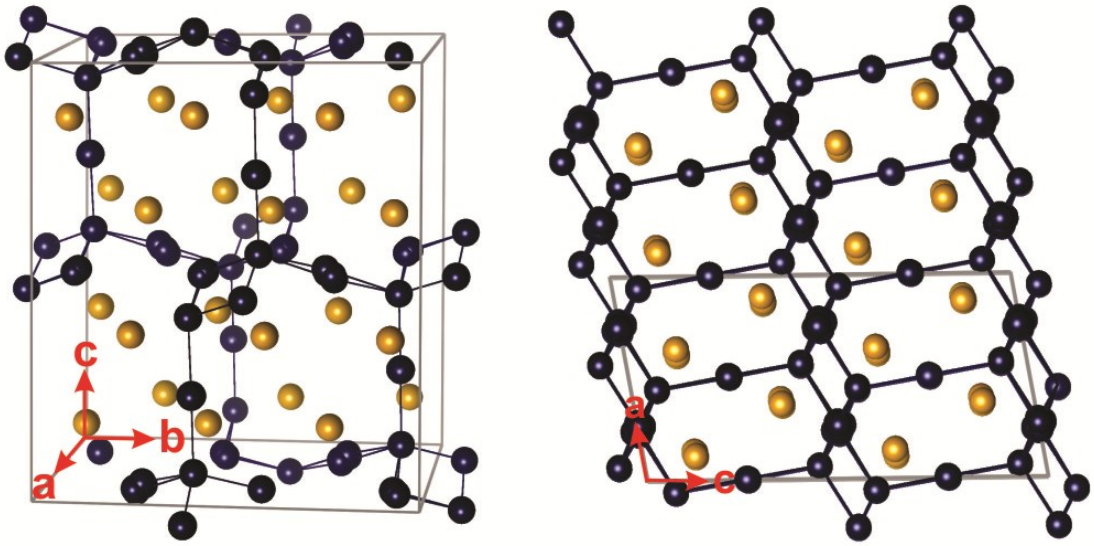

Figure S8. Calculated lithium migration path in $Li[Li_{0.33}Sn_{0.67}S_2]$. Sulfur as framework atom in yellow and voids in dark blue. The lines connecting the voids display the possible migration pathway. Note that this migration pathway consists of connected chains that cross the covalent layers.

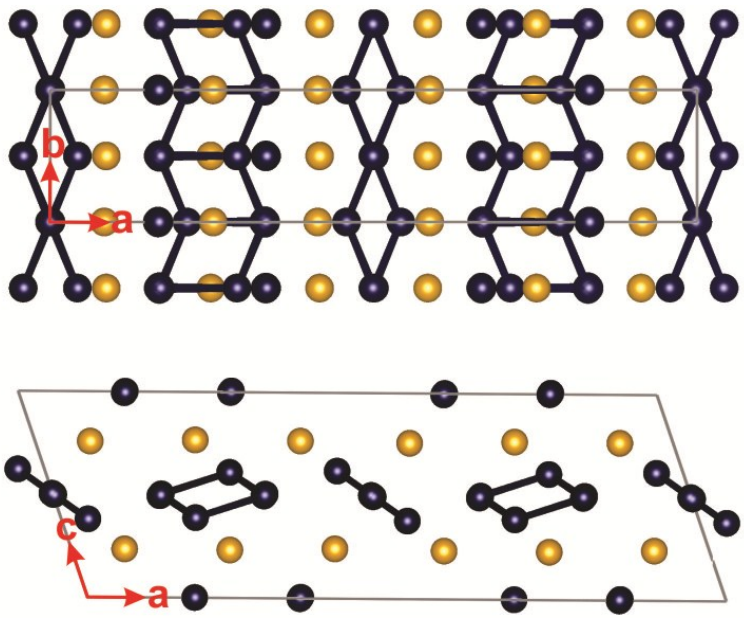

Figure S9. Calculated lithium migration path in $Li_{0.6}[Li_{0.2}Sn_{0.8}S_2]$. Sulfur as framework atom in yellow and voids in dark blue. The lines connecting the voids display the possible migration pathway. Note that this migration pathway does not cross the covalent layers.

Conductivity estimation using the Nernst-Einstein-Equation:

$$\sigma_{NMR} = \frac{D_{NMR}\, n\, z^2\, e^2}{k_B T} \qquad \textbf{(1)}$$

D_{NMR}: Diffusion coefficient determined by PFG NMR ($m^2\ s^{-1}$); n: concentration of diffusing species that take part in the ion conduction (if only interlayer Li^+ ions: $8.62 \cdot 10^{27}\ m^{-3}$, if all Li^+ ions: $1.15 \cdot 10^{28}\ m^{-3}$); z: charge number of diffusion species, here +1 for Li^+; e: elemental charge ($1.60 \cdot 10^{-19}$ C); k_B: Boltzmann constant ($1.38 \cdot 10^{-23}$ kg $m^2\ s^{-2}\ K^{-1}$), T: Temperature (293 K).

The conductivity was calculated for each PFG NMR measurement with varying Δ values. The results are listed in Table S5. We calculated σ_{NMR} for the case that – according to the TOPOS calculations - only the interlayer Li^+ ions are responsible for the conduction. Note that Δ = 10 ms is closest to the bulk conductivity and if all lithium ions would take part into the conduction σ_{NMR} would be slightly above 10^{-2} S cm^{-1}, which is in the range of the best known solid-state electrolytes.

Table S5. Conductivity determined by PFG NMR according to equation (1).

Δ / ms	D_{NMR} / m^2 s^{-1}	σ_{NMR} (only interlayer Li^+ ions) / S cm^{-1}
10	$1.7 \cdot 10^{-11}$	$9.2 \cdot 10^{-3}$
20	$1.2 \cdot 10^{-11}$	$6.5 \cdot 10^{-3}$
25	$6.7 \cdot 10^{-12}$	$3.6 \cdot 10^{-3}$
30	$7.0 \cdot 10^{-12}$	$3.8 \cdot 10^{-3}$
40	$6.5 \cdot 10^{-12}$	$3.5 \cdot 10^{-3}$
50	$3.2 \cdot 10^{-12}$	$1.7 \cdot 10^{-3}$
100	$1.7 \cdot 10^{-12}$	$9.1 \cdot 10^{-4}$

Table S6. Bulk conductivity σ of three different samples determined by PFG NMR (σ_{NMR}) and impedance spectroscopy (σ_{298K}). The samples are expected to differ in particle distribution and possibly also in their exact composition.

	σ_{NMR} / S cm^{-1}	σ_{298K} / S cm^{-1}
Sample 1	$9 \cdot 10^{-3}$	$2 \cdot 10^{-2}$
Sample 2	$3 \cdot 10^{-3}$	$4 \cdot 10^{-3}$
Sample 3*	$5 \cdot 10^{-4}$	$5 \cdot 10^{-4}$

*Partially hydrated.

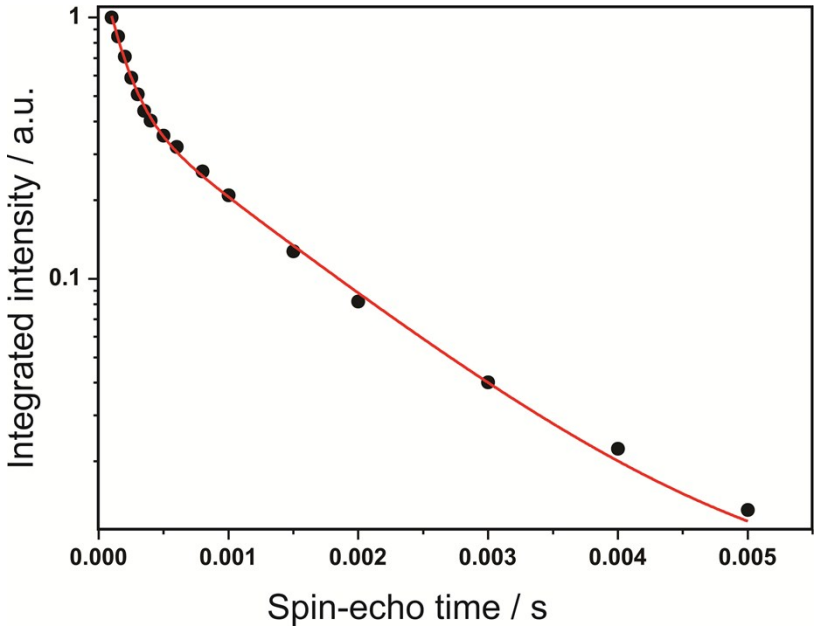

Figure S10. Signal attenuation of the ^{7}Li central transition as a function of the duration of the spin-echo time. The experimental points are fitted with a bi-exponential function characterized by spin-spin relaxation times of T_2' = 1.13 ms and T_2'' = 0.144 ms.

Estimation of the electronic contribution to the conductivity

As we did not reach the steady state we can only estimate an upper limit for the electronic contribution U_e to the conductivity. After applying a current of I = 1 nA for more than 6 h we reach a voltage of U_∞ = 163.80 mV. In the galvanostatic experiment, the sudden *IR* drop (U_0) after having switched on the current yields $U_0 = U_i + U_{contact}$ as 0.53 mV. (Note that U_i refers to the bulk response, whereas $U_{contact}$ comprises the contributions stemming from grain boundaries and contacts between particles that can be easily estimated from impedance spectra). PFG NMR data show that the bulk conductivity is on the order of $9.3 \cdot 10^{-3}$ S cm^{-1}, from which $U_i \sim 2 \cdot 10^{-4}$ mV results. The electronic transference number follows as

$$t_e = \frac{U_i}{U_i + U_e} \approx U_i / U_e = 10^{-6},$$

where

$$U_e = U_\infty - U_{contact}$$

and U_∞ is the steady state voltage.

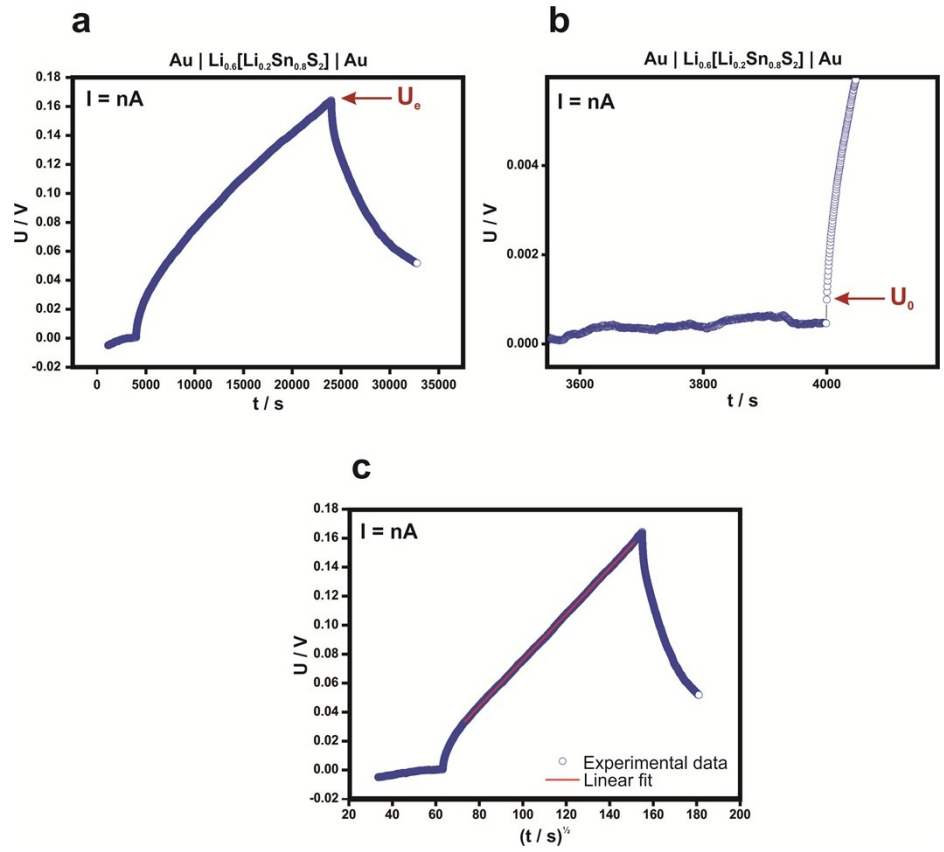

Figure S11. Electrical measurements on $Li_{0.6}[Li_{0.2}Sn_{0.8}S_2]$ performed at 298 K under argon atmosphere. (a) Full spectrum of the galvanostatic DC measurements of $Li_{0.6}[Li_{0.2}Sn_{0.8}S_2]$ without LiAl alloy. (b) Magnification of the first step after adding the current. (c) Voltage as a function of the square root of time. The maximum voltage value corresponds to U_e, the first step after adding the current corresponds to U_0.

The data collected during the transient of the polarization measurements can be used to independently support the considerations made above. The upper limit of the electronic conductivity can be estimated by considering the following expression [8], which holds for $t < \tau^{\delta}$ (τ^{δ} being the characteristic chemical diffusion time).

$$U - U_{contact} = \frac{IL}{\sigma} + \frac{\sigma_{ion}}{\sigma} \cdot \frac{IL}{\sigma_{eon}} \cdot \frac{4}{\pi^{3/2}} \sqrt{\frac{t}{\tau^{\delta}}},$$

where I is the current (1 nA) and L the diffusion length (i.e. the thickness of the sample ca. 2 mm). As the evolution of the voltage fits well the square root law and since $\sigma \cong \sigma_{ion}$ and $\tau^{\delta} > 15000$ s (Fig. S10 c), $\sigma_{eon} < 10^{-9}$ S·cm^{-1} results, which is consistent with the transference number value obtained above.

Additional impedance measurements on $Li_{0.6}[Li_{0.2}Sn_{0.8}S_2]$

1) Figure S12 shows a Nyquist plot of the complex impedance recorded using ion-blocking (Au) electrodes. In the low frequency range, a typical Warburg behavior can be recognized.

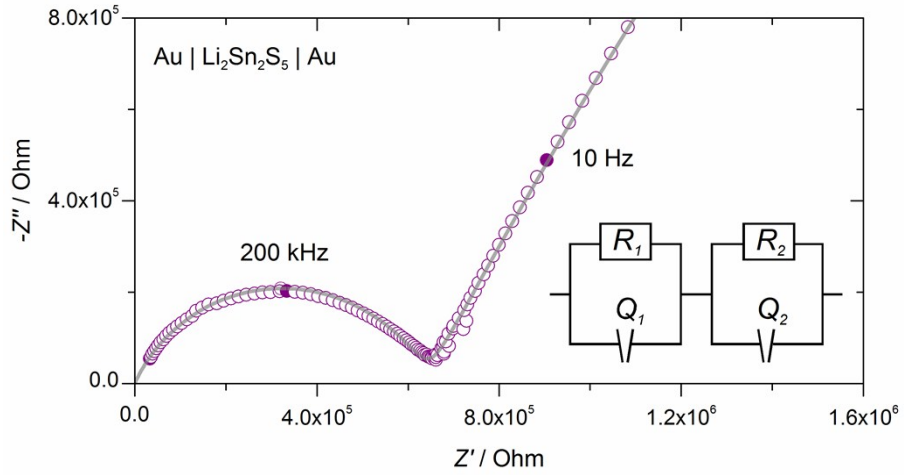

Figure S12. Nyquist plot of the complex impedance of the $Li_{0.6}[Li_{0.2}Sn_{0.8}S_2]$ sample acquired using Au electrodes. The open circles correspond to the experimental data, while the grey line was obtained by fitting the data with the equivalent circuit shown in the bottom right corner.

2) In Figure S13 an additional impedance spectrum is presented, which was acquired using an extended frequency range, namely up to 10 MHz. Here, despite the increased noise, the transition to the bulk semi-circle (at high frequency) can be clearly recognized.

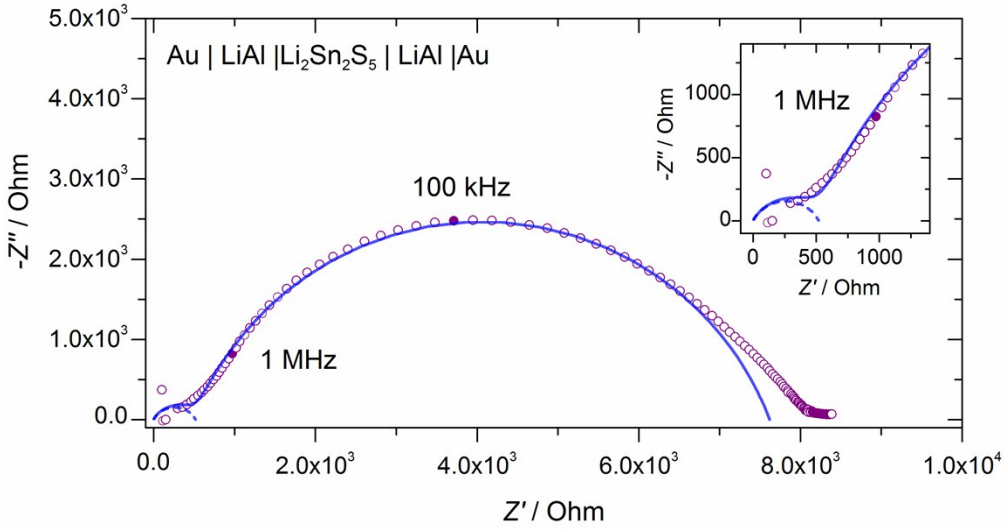

Figure S13. Nyquist plot of the complex impedance acquired in the non-blocking configuration Au|LiAl|$Li_{0.6}[Li_{0.2}Sn_{0.8}S_2]$|LiAl|Au at frequencies up to 10 MHz indicating the transition to the bulk response. The inset highlights the frequency range above 1 MHz and the dashed line correspond to the high frequency contribution. The high frequency behavior demonstrates that the high frequency intercept referred to in the main text is not an artefact of inductive phenomena.

Electrical measurements on $Li[Li_{0.33}Sn_{0.67}S_2]$

Electrical measurements were performed also on the related compound $Li[Li_{0.33}Sn_{0.67}S_2]$ under the same conditions used for $Li_{0.6}[Li_{0.2}Sn_{0.8}S_2]$. Figure S14(a) displays the Nyquist plot of the complex impedance, which can be fitted (grey line) by the equivalent circuit consisting of 3*RQ* elements, where *Q* is a constant phase element, whose capacitance is defined as $C = (R^{1-n}Q)^{1/n}$ (*n* is an additional fitting parameter). The resulting bulk conductivity is $6 \cdot 10^{-8}$ S cm^{-1}.

The results of the corresponding d.c. galvanostatic measurement are shown in Figure S14b. It is noteworthy that the value of the low frequency intercept with the *x*-axis of Figure S14a is in good agreement with the resistance value resulting from the d.c. measurement shown in Figure S14b.

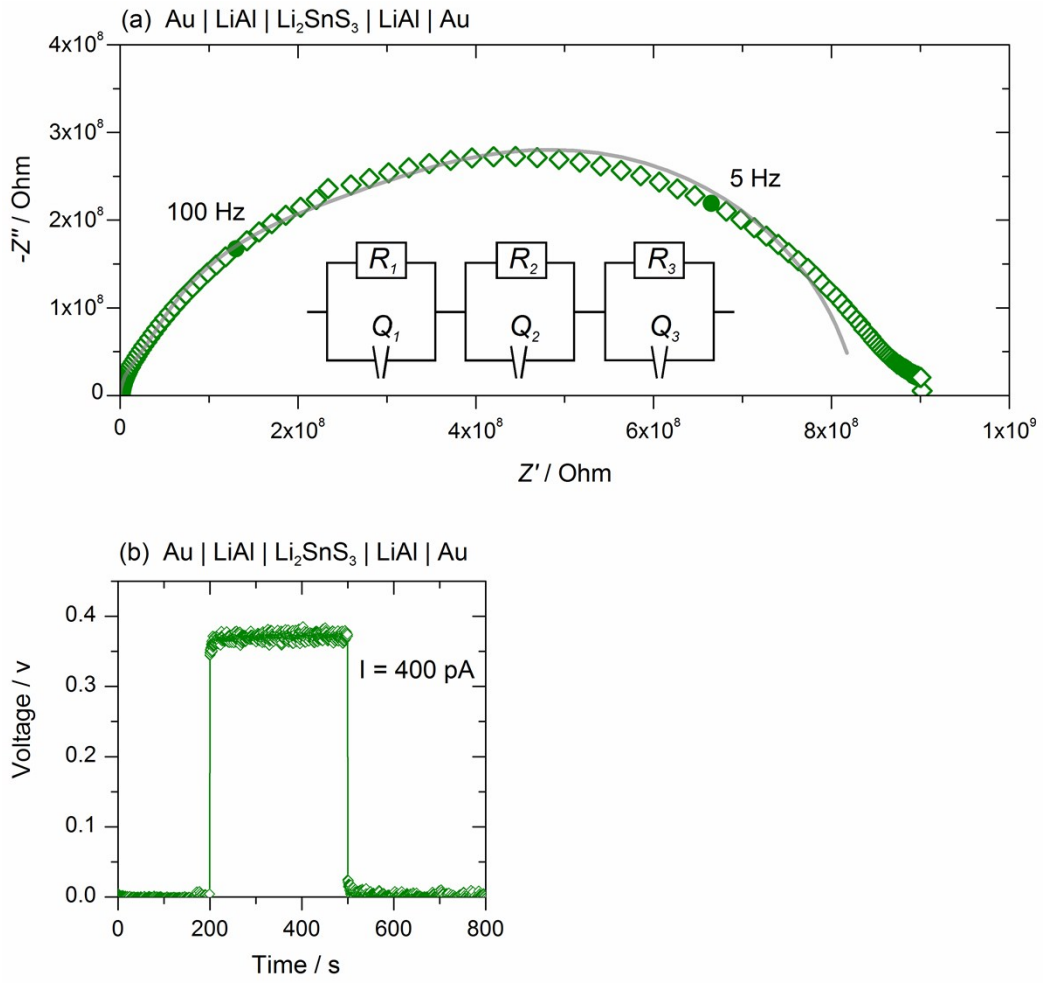

Figure S14. (a) Nyquist plot of the complex impedance and (b) d.c. galvanostatic measurement of $Li[Li_{0.33}Sn_{0.67}S_2]$. In (a) the open diamonds correspond to the experimental data whereas the grey line represents the fitting, which was obtained by using the equivalent circuit shown in the figure.

Literature:

[1] A. Kuhn, T. Holzmann, J. Nuss and B. V. Lotsch, *J. Mater. Chem. A,* 2014, **2**, 6100.

[2] R. K. Harris, E. D. Becker, S. M. Cabral De Menezes, P. Granger, R. E. Hoffman and K. W. Zilm, *Pure and Applied Chemistry,* 2008, **80**, 59.

[3] A. Bielecki and D. P. Burum, *J. Magn. Reson. Ser. A,* 1995, **116**, 215.

[4] D. Massiot, F. Fayon, M. Capron, I. King, S. Le Calvé, B. Alonso, J. O. Durand, B. Bujoli, Z. Gan and G. Hoatson, *Magn. Reson. Chem.,* 2002, **40**, 70.

[5] J. Rohonczy, Bruker BioSpin GmbH: Rheinstetten, Germany, 2009.

[6] T. Pietrass and F. Taulelle, *Magn. Reson. Chem.,* 1997, **35**, 363.

[7] T. Pietrass and F. Taulelle, *J. Phys. Chem. B,* 1997, **101**, 6715.

[8] J. Maier, *Physical Chemistry of Ionic Materials*, John Wiley & Sons, Chichester England (2004).

[9] J. A. Brant, D. M. Massi, N. A. W. Holzwarth, J. H. MacNeil, A. P. Douvalis, T. Bakas, S. W. Martin, M. D. Gross and J. A. Aitken, *Chem. Mater*., 2015, **27**, 189.